Effect of stratospheric aerosol injection strategy on radiative forcing and precipitation

Master's Thesis, 23.8.2023

Author:

Liisa Miettinen

Supervisor:

Anton Laakso (Finnish Meteorological Institute)
Vesa Apaja

UNIVERSITY OF JYVÄSKYLÄ
DEPARTMENT OF PHYSICS

Abstract

Miettinen, Liisa
Effect of stratospheric aerosol injection strategy on radiative forcing and precipitation
Master's thesis
Department of Physics, University of Jyväskylä, 2023, 47 pages.

Constant and varying injection strategies for stratospheric aerosol intervention with sulfur are compared in terms of radiative forcing and fast precipitation response. Sulfur is injected continuously at the equator in the constant strategy while the injection area is varied spatially and temporally in the varying strategy. Injection magnitudes between 2 - 100 $\mathrm{Tg(S)yr^{-1}}$ are simulated with EC-Earth3 using aerosol modules M7 and SALSA. CO_2 compensation capacities of both strategies are also considered. The varying strategy was found to produce a stronger radiative forcing and smaller precipitation due to the fast precipitation response compared to the constant strategy above $10\,\mathrm{Tg(S)yr^{-1}}$ injection rates. Aerosol fields simulated with SALSA produced stronger radiative forcing compared to M7 in majority of the scenarios, however no clear trend was observed in fast precipitation response in terms of aerosol module. CO_2 compensation capacities of both injection strategies were similar for simulations using SALSA below $20\,\mathrm{Tg(S)yr^{-1}}$ injection rates, however the varying strategy was more effective than the constant strategy in simulations using aerosol fields simulated with M7.

Keywords: Geoengineering, stratospheric aerosol intervention, radiative forcing, fast precipitation response, CO_2 compensation

Tiivistelmä

Miettinen, Liisa
Yläilmakehän aerosoli-injektioiden vaikutus säteilypakotteeseen ja sateisuuteen
Pro gradu -tutkielma
Fysiikan laitos, Jyväskylän yliopisto, 2023, 47 sivua

Tutkielmassa tarkastellaan yläilmakehän rikki-injektioihin perustuvaa vakio- ja vuodenajan mukaan vaihtelevaa ilmastonmuokkausstrategiaa. Vakiostrategiassa rikkiä lähetetään jatkuvasti päiväntasaajalle, ja vaihtelevassa strategiassa rikki-injektioiden paikka vaihtelee vuodenajan mukaan. Injektioskenaarioita simuloidaan EC-Earth3 ilmastomallin, ja SALSA ja M7 aerosolimoduulien avulla, missä lähetetyn rikin määrä vaihtelee 2 - 100 $\mathrm{Tg(S)yr^{-1}}$ välillä. Näiden lisäksi tutkitaan kummankin strategian kykyä kompensoida ilmakehän hiilidioksidipitoisuuden aiheuttamaa lämpenemistä. Vuodenajan mukaan vaihteleva strategia aiheutti voimakkaamman säteilypakotteen ja pienemmän muutoksen sateisuudessa kun injektiomäärä oli pienempi kuin $10\,\mathrm{Tg(S)yr^{-1}}$. Enemmistö SALSA aersolimoduulilla simuloiduista hiukkaskentistä tuotti voimakkaampia säteilypakotteita verrattuna M7:n simulaatioihin. Sateisuudessa ei esiintynyt aerosolimoduuliin liittyviä selkeitä eroja. Alle $20\,\mathrm{Tg(S)yr^{-1}}$ injektiomäärillä kumpikin injektiostrategia oli yhtä tehokas SALSA aerosolimoduulilla, mutta vaihteleva strategia oli tehokkaampi M7 aerosolimoduulilla simuloiduilla aerosolikentillä.

Avainsanat: Ilmastonmuokkaus, yläilmakehän rikki-injektio, säteilypakote, sateisuus, hiilidioksidipitoisuuden kompensaatio

Preface

This thesis was written during the 2022-2023 academic year in collaboration with the Finnish Meteorological Institute. I'd like to thank Prof. Anton Laakso first and foremost for the great quality of supervision during the project. I'd also like to thank the Atmospheric Modelling group, and the Head of Group Prof. Harri Kokkola. In addition to learning about geoengineering and atmospheric models, I was also able to get a glimpse of the group's other research during weekly meetings. Atmospheric physics is a great combination of phenomena that are both theoretically challenging, computationally interesting and applicable to daily life.

Senior Researcher Vesa Apaja was my supervisor from University of Jyväskylä, and I'd like to thank him for his help with the Python code and other practical matters. Lastly I want to thank all my friends in our student room "Origo" for all the conversations shared over a few (or quite a few) cups of coffee.

Jyväskylä 23.8.2023

Liisa Miettinen

Contents

1 Introduction

The atmospheric concentration of greenhouses gases (GHG) has increased due to fossil fuel emissions. This disrupts the Earth's energy balance because more energy gets absorbed by the atmosphere, which causes it to heat up and emit thermal radiation back to the surface. The consequence of this imbalance is global warming which has serious long-term effects such as an increase in extreme weather events, loss of endangered species and unique ecosystems, loss of continental ice sheets, and changes in the ocean-atmosphere system which could impact water resource availability. [1][2, p. v]

The difference between the amount of solar radiation absorbed by the Earth and the radiation emitted into space determines the Earth's temperature. An imbalance in this situation is called radiative forcing which results in a temperature adjustment until the balance is restored [2, p.3]. Human activity has caused a significant increase in the atmospheric CO_2 concentrations which in turn has caused an increase in the energy retained by the Earth [2, p.2]. The radiative forcing caused by human activity is estimated to be $1.6\,\mathrm{W/m^2}$, and about half of this has been balanced by global warming so far [2, p.4].

While reducing global GHG is the main priority since it's the root cause of global warming, geoengineering methods are being developed as a "plan B" for reducing its effects [2, p. v]. These methods can be classified into carbon dioxide removal methods and solar radiation management [2, p. ix]. This thesis focuses on stratospheric aerosol intervention (SAI) with sulfur, which falls under solar radiation management [2, p. 29].

SAI using sulfur involves creating a reflective aerosol layer in the stratosphere by using sulfur injections. This method produces effects similar to the effects of volcanic eruptions where large amounts of SO_2 is released into the atmosphere. SO_2 oxidizes into sulfate aerosols which are effective at scattering light because they're about the same size as visible light (with a typical radius of $0.5\,\mu\mathrm{m}$) and they have a single scatter albedo (fraction of sunlight that is diffusively reflected) of about 1[3][4].

These aerosols cause a reflective aerosol field to form, thus effectively decreasing the amount of visible light and UV radiation reaching the Earth's surface. The end result is a cooling effect that can last 2-3 years [3].

While large-scale volcanic eruptions such as the Mt. Pinatubo eruption in 1991 provide valuable information about the possible effects of SAI, drawing conclusions about the effectivity of SAI from volcanic eruption data is not straightforward. SAI involves continuous injection whereas the gases from a volcanic eruption are released in a relatively short time frame. In addition to this, SAI would affect the size distribution of aerosol particles differently because sulfur is is injected continuously to an existing particle field. [5]

For this reason climate model simulations are very useful for researching the possible effects of SAI. This thesis focuses on expanding the work done in [5], where a constant injection strategy at the equator was used for the simulations. A temporally and spatially varying injection strategy was hypothesized to be more effective compared to a constant equatorial injection strategy in [6]. Effectiveness of a strategy is defined as a stronger cooling effect and less disruption in precipitation. In order to test this hypothesis, I analyze the data obtained from these simulations, and run new simulations based on a temporally and spatially varying injection strategy using the EC-Earth3 Earth System Model.

The main goal of this work is to determine whether the spatially and temporally varying injection strategy produces a stronger cooling effect, and the effect of this strategy on rainfall. In addition to this, the effect of using a modal or a sectional aerosol module in the simulations is also investigated.

2 Theoretical background

2.1 Radiative forcing

A compact definition for radiative forcing is the instantaneous flux change at the top of the atmosphere (TOA). It can also be defined in terms of the instantaneous flux change at the border between the troposphere and stratosphere, however the TOA definition is used in this thesis. [7]

Manually applied radiative forcing, for example SAI using sulfur, causes a radiative response in the climate that attempts to restore the energy balance [8]. If we denote the applied forcing by F and the radiative response by H, the net heat flux N can be written as

$$N = F - H, \tag{1}$$

where F and H values are both global annual averages in Wm^{-2} [8]. The radiative response H is related to the global average surface temperature T in the following way

$$H = \alpha\, \Delta T, \tag{2}$$

where the climate response parameter α is the mean surface temperature response to a radiative perturbation, and it is assumed to be constant during the simulations. If the magnitude of applied forcing remains constant for several years, the radiative forcing F can be calculated by regressing the net heat flux N against ΔT, resulting in

$$N(t) = F - \alpha \Delta T(t), \tag{3}$$

where we combine equations (1) and (2) [8]. From equation (3) we can conclude that the y axis intercept ($\Delta T = 0$) of a $N(\Delta T)$ graph gives the amount of radiative forcing F. [8][9]

Now we can examine how the manually applied radiative forcing F_{SAI} can compensate for the radiative forcing F_{CO_2} that's caused by the atmospheric CO_2 concentration.

F_{CO_2} and the CO_2 concentration C are related by

$$F_{CO_2} = a \log\left(\frac{C}{C_0}\right), \tag{4}$$

where C_0 is the pre-industrial CO_2 concentration in ppm [10]. The known value of a is $5.35\,\mathrm{Wm}^{-2}$ and it is also calculated from model data in section 3.4 [10]. Equation (4) can be used for calculating the radiative forcing that's needed to offset a particular CO_2 concentration. In order to compensate a given F_{CO_2}, we need a manually applied radiative forcing F_{SAI} with the same magnitude and opposite sign. F_{SAI} is negative and F_{CO_2} is positive by convention, so $-F_{SAI} = F_{CO_2}$ is needed for compensation. Replacing F_{CO_2} with $-F_{SAI}$ and rearranging equation (4) results in

$$C = C_0\, e^{\left(\frac{-F_{SAI}}{a}\right)}, \tag{5}$$

which allows us to calculate the CO_2 concentration a given SAI with sulfur scenario would be able to compensate for.

2.2 Precipitation response

The overall precipitation response P is the sum of the slow precipitation response P_{slow} and the fast precipitation response P_{fast}. P_{slow} is caused by the global mean surface temperature change, and it is slower because the Earth's surface, which is mostly water, reacts to temperature changes slowly compared to surface level air. For this reason the fast precipitation response occurs within weeks, and the slow precipitation response occurs withing months after radiative forcing is applied. [11]

This thesis focuses on the fast precipitation response P_{fast}. This response is mainly caused by the change in atmospheric absorption. In SAI, the sulfur injections change the amount of energy transferred between TOA and the Earth's surface. This affects the amount of evaporation which in turn affects precipitation. [12]

The slow precipitation response is linearly proportional to temperature change which can be written as

$$P_{slow} = \gamma \Delta T, \tag{6}$$

where the constant γ measures the change in precipitation per ΔT in % K^{-1} [11]. Since $P = P_{fast} + P_{slow}$ by definition, we get

$$P = P_{fast} + \gamma \Delta T \tag{7}$$

by using equation (6) and substituting $\gamma \Delta T$ for P_{slow}. As a result, the fast precipitation response can be calculated with equation (7) by regressing P against ΔT and taking the y-intercept of the $P(\Delta T)$ graph.

3 Methods and materials

3.1 ECHAM-HAMMOZ and EC-Earth3

This thesis uses simulation data obtained from ECHAM6.3-HAM2.3-MOZ1.0 (shortened to ECHAM-HAMMOZ) and EC-Earth3. ECHAM-HAMMOZ is an aerosol-climate model that consists of the general circulation model ECHAM6.3, the Hamburg Aerosol Model HAM2.3 and the gas-phase tropospheric and stratospheric chemistry module MOZ1.0. EC-Earth3 is an Earth System Model with a climate model core composed of physical models for the atmosphere (IFS), ocean (NEMO), ocean biogeochemistry (PISCES) and land (LPJ-GUESS). [13] [5] [14]

ECHAM6.3 is a general circulation model developed by the Max Planck Institute for Meteorology. It calculates temperature, surface pressure, vorticity (pseudovector field that describes the tendency to rotate) and divergence in addition to different processes such as diffusion, convection and turbulence. The Hamburg Aerosol Model HAM2.3 parametrizes aerosol processes such as emission, nucleation and condensation. Two different aerosol microphysics modules can be used with HAM2.3: The modal module M7 and the sectional module SALSA, which are the topic of section 3.2. MOZ is a gas phase chemistry scheme that can be run with HAM. It calculates different heterogeneous chemical reactions that occur in the atmosphere such as the formation of HO_2 and the uptake of HO_2, NO_3, NO_2, HNO_3 and N_2O_5. [13]

The other climate model used in this thesis is EC-Earth3 which has different coupled configurations for climate processes. IFS (Integrated Forecast System) simulates the relevant processes in the atmosphere similarly to ECHAM. NEMO (Nucleus for European Modelling of the Ocean) simulates ocean circulation and the sea ice. PISCES (Pelagic Interactions Scheme for Carbon and Ecosystem Studies) simulates the nutrient cycle and the marine carbon cycle. LPJ-GUESS (Lund-Potsdam-Jena General Ecosystem Simulator) simulates land biogeochemistry and vegetation. [14]

3.2 Aerosol microphysics modules SALSA and M7

Modelling aerosol dynamics is important for the calculation of radiative forcing since it is very sensitive to particle size. For example, the scattering efficiency peaks when the size of the particle is close to the wavelength of light. There are different approaches to representing aerosol size distributions, however the sectional and modal approaches are the most common. In a sectional approach, the particle size distribution is approximated by using discrete sections called size bins. In the modal approach, particle size distribution is approximated with analytical functions. [15]

M7 uses lognormal distribution, a continuous probability distribution of a random variable whose logarithm is normally distributed, to approximate the aerosol population by their mass and number. Water soluble particles are represented by four lognormal modes and water insoluble particles are represented by three lognormal modes. The sum of these modes gives the total distribution. [16]

SALSA (a Sectional Aerosol module for Large Scale Applications) is a sectional aerosol dynamics module. It uses size bins with different size resolutions. For example, a lower size resolution can be used for regions that are less relevant to the research problem. The usage of size bins also simplifies the treatment of different aerosol types and microphysical processes because these properties are closely related to particle size. [17]

Particles are divided into two sub-ranges which contain 10 size bins for water soluble particles (which span over both sub-ranges) and 7 size bins for water insoluble particles (contained in sub-range 2). Sub-range 1 is made up of particles with a diameter between $3\,\text{nm} - 50\,\text{nm}$, and sub-range 2 is made up of particles with a diameter between $50\,\text{nm} - 10\,\mu\text{m}$. These sub-ranges contain different chemical components and externally mixed groups of particles. [17]

3.3 Model configuration

Supercomputer Puhti (a part of CSC, IT Center for Science) was used for running the simulations [18]. At first ECHAM-HAMMOZ, SALSA and M7 were used to simulate the entire process particle fields go through (particle formation after injection, interactions between particles, movement and removal from the atmosphere). The optical properties of particles that affect radiation are also calculated at this stage. However the ECHAM-HAMMOZ simulations don't include oceans, so the effects on climate can't be investigated with these simulations. In the second stage, the optical properties of aerosol fields simulated at the first stage are used as inputs for the EC-Earth3 simulations since EC-Earth3 takes oceans and sea ice into account.

In [5] the simulations were done with ECHAM-HAMMOZ where the sea surface temperature and sea ice were fixed to year 2005 levels. Resolution of the simulation was T63L95, which is approximately a 200 km×200 km horizontal grid with 95 vertical layers. The chemistry model MOZ was not used because it would significantly increase the computational time, and its impact on the stratospheric sulfur field was small compared to other microphysical processes. [5]

The EC-Earth3 simulations use T255L91 resolution for IFS which is approximately a 80 km × 80 km horizontal grid with 91 vertical levels, and ORCA1L75 resolution for NEMO which is approximately a 135 km × 135 km horizontal grid with 85 vertical levels. The simulation start date is 01/01/1990 and the duration of the simulation is 60 years. Initial conditions of the simulations are set to pre-industrial levels except the variable that's being investigated (SAI or CO_2 level).

3.4 Data sets and scenarios

The data sets used in this thesis are shown in table 1. The simulation results are initially stored in GRIB (Gridded binary) file format. Then the yearly average of each variable is calculated and the data is converted to NetCDF file format. The variables of interest are T2M (2 meter temperature in Kelvin), TSR (top solar radiation in $Wm^{-2}s$), TTR (top thermal radiation in $Wm^{-2}s$) and TP (total precipitation in m).

Data set I is a control scenario without SAI that represents pre-industrial conditions. The change in different variables such as TSR and TTR are calculated with respect to this data set. Data sets I, II, III and IV originate from [19] while V and VI are

the results of new simulations done during the this project.

Table 1. Data sets used in this work.

Set	Name	Description
I	EXPI	Control scenario with pre-industrial conditions. CO_2 concentration is 284.5 ppm.
II	EX2C, EX3C, EX4C	Scenarios where the CO_2 concentration is 569 ppm, 853.5 ppm and 1138 ppm respectively.
III	ES2M, ES5M, E10M, E20M, E50M, ESCM	Constant injection scenarios where aerosol fields simulated with M7 and are used. Injection rates are 2, 5, 10, 20, 50 and 100 Tg(S)yr^{-1}respectively.
IV	ES2S, ES5S, E10S, E20S, E50S, ESCS	Constant injection scenarios where aerosol fields simulated with SALSA are used. Injection rates are 2, 5, 10, 20, 50 and 100 Tg(S)yr^{-1} respectively.
V	TS2M, TS5M, T20M, T50M	Varying injection scenarios where aerosol fields simulated with M7 and are used. Injection rates are 2, 5, 20 and 50 Tg(S)yr^{-1} respectively.
VI	TS2S, TS5S, T20S,T50S	Varying injection scenarios where aerosol fields simulated with SALSA and are used. Injection rates are 2, 5, 20 and 50 Tg(S)yr^{-1} respectively.

Data sets III and IV were obtained from simulations where sulfate was continuously injected at the equator. This will be referred as the constant injection strategy. In this strategy, sulfate is injected continuously between 10 °N and 10 °S parallels at a height of 20-22 km. Data sets V and VI were obtained from simulations done with a varying injection strategy. In this strategy, sulfate is injected continuously to a 20° wide area between 40 °N and 40 °S parallels at a height of 20-22 km. The injection location varies by the season, with the northernmost 20° area injections in May.

The magnitude of injection in data sets III, IV, V and VI is indicated by the number in each name i.e. 2 Tg(S)yr^{-1} was injected in ES2M and 50 Tg(S)yr^{-1} was injected in T50M. As an exception, 100 Tg(S)yr^{-1} scenarios are marked with letter C as in ESCS and ESCM. The aerosol module is marked at the end of the simulation name

with S for SALSA and M for M7.

The linear regression method described in section 2 is done using Python. TTR and TSR values are divided by the time-step of the simulation $(60 * 60 * 3.0)$ in order to get the mean value, because the instant value of the variable is added to the output at each time-step. The control data set's (EXPI in table 1) TTR, TSR and T2M values are subtracted from the TTR, TSR and T2M values of data sets III, IV, V and VI. Then the TTR and TSR are plotted as a function of T2M.

TTR and TSR correspond to the net heat flux N in (1) and T2M corresponds to ΔT in (2). We get the radiative forcing F by regressing TTR, TSR or their sum against T2M using equation (3) and taking the y-axis intercept value.

The data sets I and II and equation (3) are used to calculate the radiative forcing caused by different CO_2 concentrations. The constant a in equation (4) is calculated with a logarithmic fit to the $F(C)$ graph. After this, the total radiative forcing F_{TOT} is used as F_{SAI} in equation (5) in order to calculate the CO_2 compensation capacities of each scenario in data sets III, IV, V and VI.

The calculation of the fast precipitation response follows a similar pattern where the T2M values of the control data set are subtracted from the T2M values of data sets III, IV, V and VI. The TP values of the control data set are divided by the TP values of data sets III, IV, V and VI because the percentage change in the fast precipitation response is easier to conceptualize than the absolute change. Then the fast precipitation response P is calculated by regressing TP against against T2M as described in equation (7) and taking the y-axis intercept.

3.5 Systematic uncertainties

The methods used in this thesis rely on the assumption that climate change is proportional to radiative forcing, which is a widely used assumption by both Intergovernmental Panel on Climate Change and World Meteorological Organization. It is based on climate simulations using different climate models where increasing the amount of CO_2 in the atmosphere was found to be proportional to the change in surface temperature. The interpretation was that although different climate models have responses with varying magnitudes due to differences in climate sensitivity, the climate response is proportional to radiative forcing. In particular, the climate

response is proportional to radiative forcing when the it is calculated after the stratospheric temperature has adjusted to the applied forcing. [7]

The scenarios with a $20\,\mathrm{Tg(S)yr^{-2}}$ to $100\,\mathrm{Tg(S)yr^{-2}}$ injection rate are considered extreme scenarios. A $3\,\mathrm{Tg(S)yr^{-2}}$ to $10\,\mathrm{Tg(S)yr^{-2}}$ injection rate is considered more realistic for restoring the Earth's energy balance [5]. Some of the extreme scenarios caused a significant and sudden sea level increase at different locations in EC-Earth3, which crashed the simulation. This caused delays in obtaining data and as a result, some scenarios contain less than 60 data points. This problem was exacerbated by the increased computation time in simulations using the SALSA module. TS5M and T20M have 59 data points, TS2S, TS5S and T20S have 20 data points and T50S has 16 data points. The exact cause of the EC-Earth3 model instability in larger injection rate scenarios is unclear, and it is outside the scope of this thesis.

4 Results

4.1 The injection strategy's effect on radiative forcing

The linear regression graphs for the TSR and TTR values for both injection strategies are given in appendix A figures 9, 10,11 and 12. SALSA and M7 results are shown separately for both strategies, and the TTR and TSR results are calculated separately. The y-axis intercepts, which give the radiative forcing F as described in equation (3), are shown in figure 1.

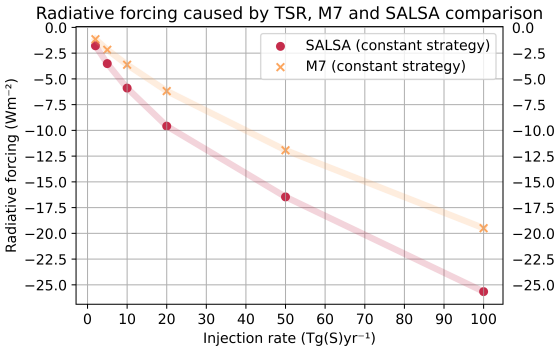

(a) F_{TSR}, constant injection strategy.

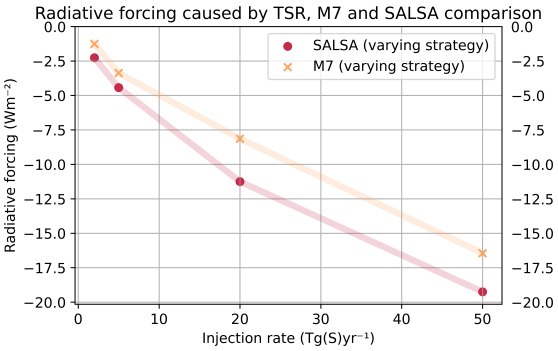

(b) F_{TSR}, varying injection strategy.

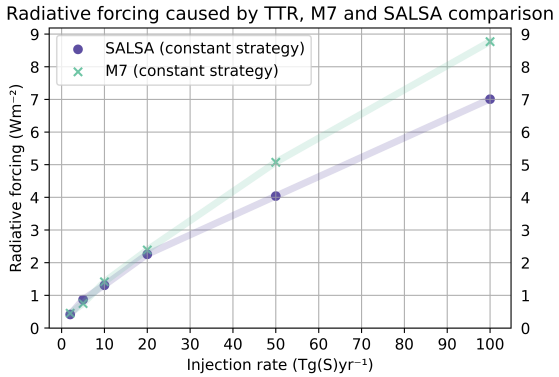

(c) F_{TTR}, constant injection strategy.

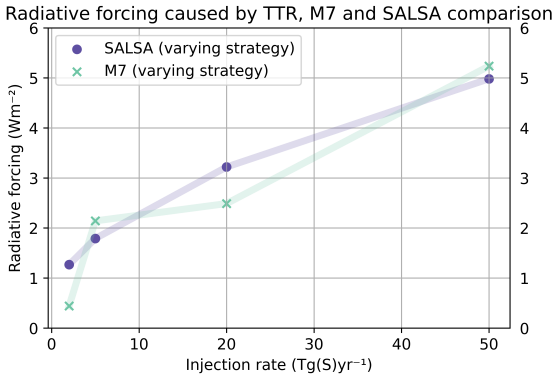

(d) F_{TTR}, varying injection strategy.

Figure 1. F derived from TSR (F_{TSR}) and F derived from TTR (F_{TTR}) as a function of injection rate for both injection strategies. M7 and SALSA results are shown separately in scatter plots. Light colored lines are added for easier comparison.

The choice of aerosol module affects the radiative forcing derived from both TSR and TTR. The difference between results from different modules increase with larger injection rates in all cases except the varying strategy's F_{TTR} as seen in figure 1. The difference between results from different modules is larger for the constant injection strategy compared to the varying injection strategy. While TSR radiative forcing is consistently larger for M7 in both injection strategies, this is not true for TTR radiative forcing.

The linear regression graphs for the total radiative forcing are shown in figures 15 and 16, and the y-axis intercepts of these graphs are shown in figure 2. $|F_{TOT}|$ is larger for SALSA in both injection strategies, and the difference between results from different modules is larger for the constant injection strategy as seen in figure 2.

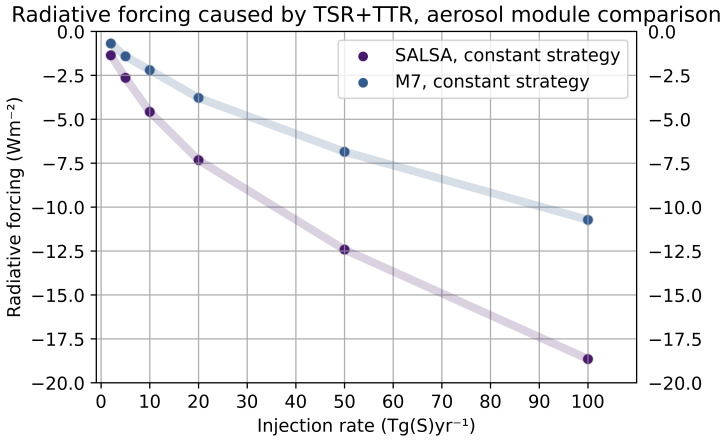

(a) F_{TOT}, constant injection strategy.

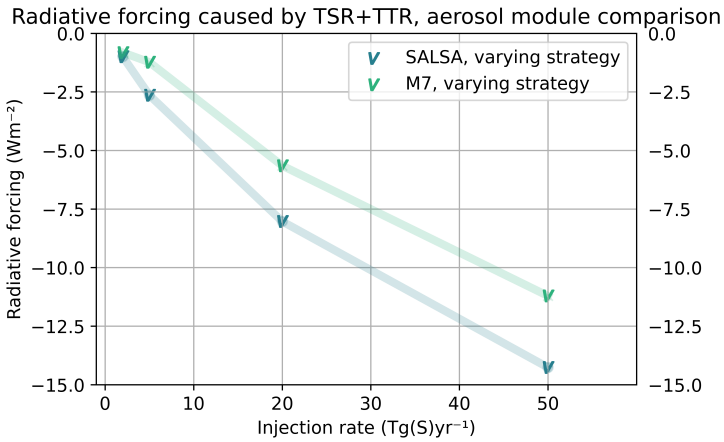

(b) F_{TOT}, varying injection strategy.

Figure 2. Total radiative forcing F_{TOT} as a function of injection rate for both injection strategies with M7 and SALSA results shown separately.

The linear regression graph used for calculating the radiative forcing caused by different CO_2 concentrations is given in figure 3a. The y-axis intercepts of this graph are shown in figure 3b with the control scenario EXPI at the origin. The logarithmic function in equation 4 was fitted to these data points. The fit parameter corresponds to the constant a in 4, which was $5.3025\,\mathrm{Wm}^{-2}$. This is close to the known value of $a = 5.35\,\mathrm{Wm}^{-2}$ [10].

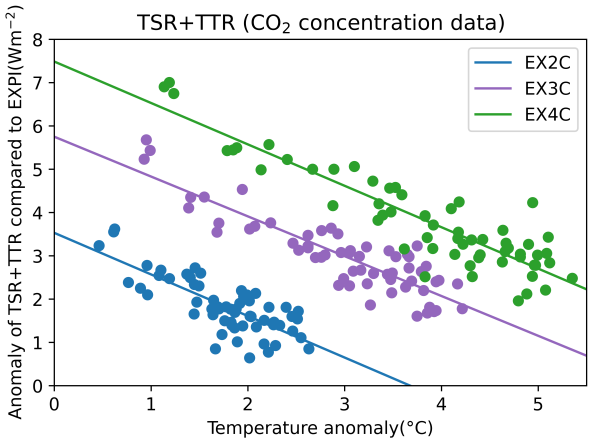

(a) Linear regression of TSR+TTR against T2M for data set II.

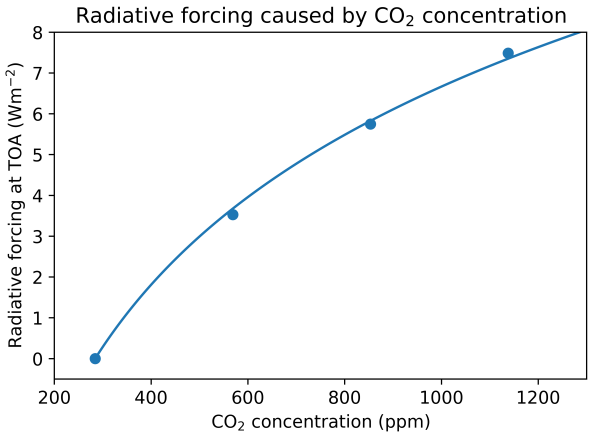

(b) Radiative forcing at TOA as a function of CO_2 concentration.

Figure 3. Dependence of radiative forcing on the atmospheric CO_2 concentration.

The linear regression graphs for the total radiative forcing F_{TOT} are given in appendix A figures 15 and 16. Figure 4 shows the injection rate needed to compensate for different CO_2 concentrations.

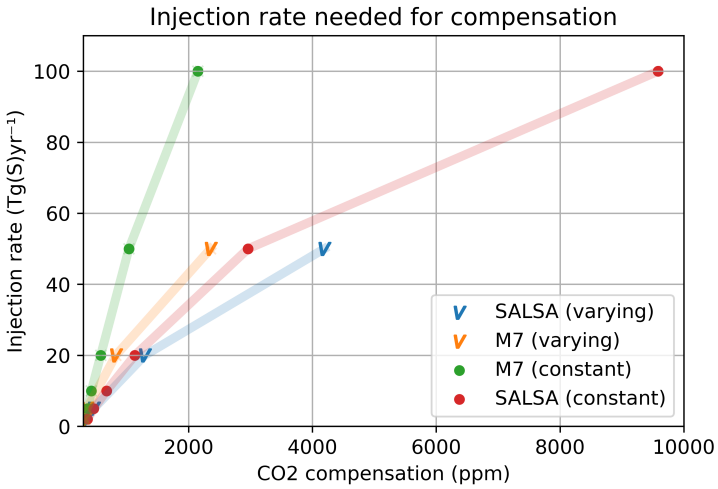

(a) Injection rate needed to compensate for a given CO_2 concentration.

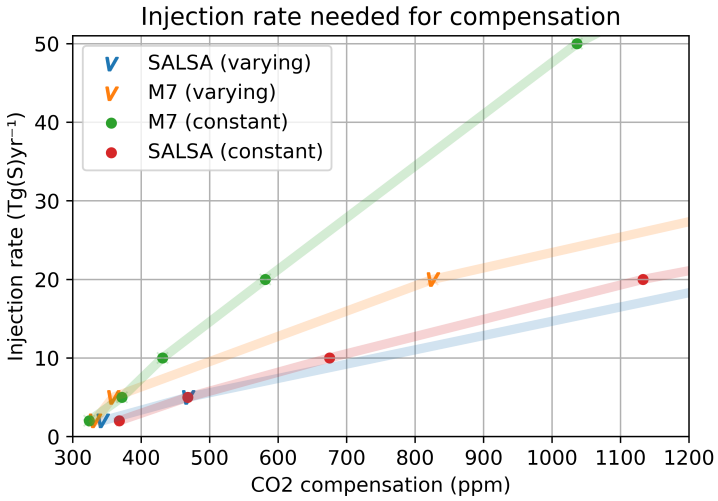

(b) Figure 4a with the x-axis restricted to 1200 ppm in order to show the smaller injection scenarios more clearly.

Figure 4. The CO_2 concentration each injection scenario would be able to compensate for. Aerosol modules and injection strategies shown separately. Numerical values are given in appendix B table 2.

The varying strategy is overall more effective at compensating CO_2 in M7 simulations, however the results are similar for both strategies in SALSA simulations at injection rates below 10 $Tg(S)yr^{-1}$. The simulations differ significantly for injection rates above 10 $Tg(S)yr^{-1}$. For example in table 2 the injection rate 20 $Tg(S)yr^{-1}$ is able to compensate for 1133 ppm (constant strategy, SALSA), 1293 ppm (varying strategy, SALSA), 581 ppm (constant strategy, M7) and 826 ppm (varying strategy, M7). The varying strategy is able to compensate for about 12% more CO_2 compared to the

constant strategy for aerosol fields simulated with SALSA, and the varying strategy is able to compensate for about 29% more CO_2 than the constant strategy for aerosol fields simulated with M7.

4.2 The injection strategy's effect on precipitation

The linear regression graphs for the TP values for both injection strategies are given in appendix A figures 13a, 13b, 14a and 14b. The y-axis intercepts (which give the fast precipitation response P) of the aforementioned linear regression graphs are shown in figure 5.

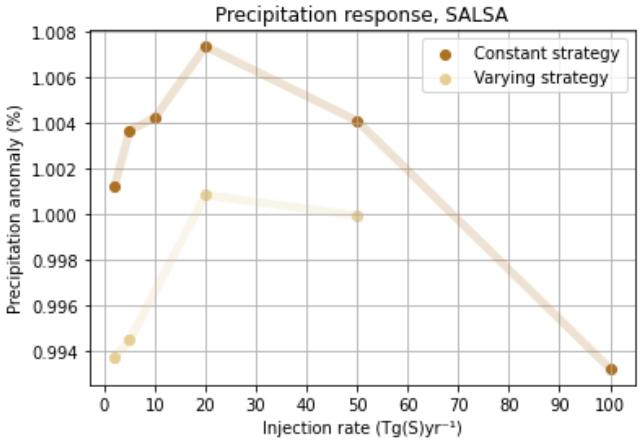

(a) P_{SALSA} for both injection strategies.

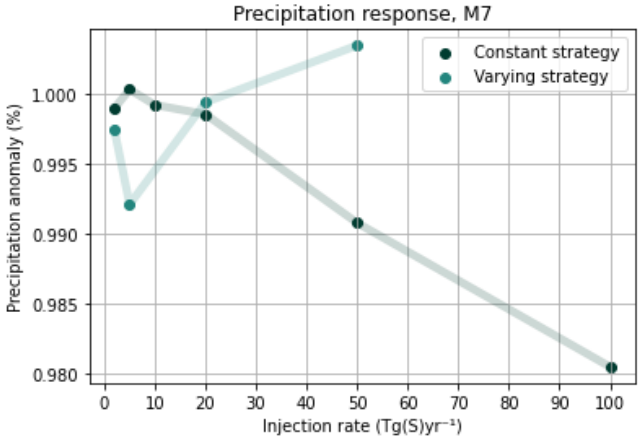

(b) P_{M7} for both injection strategies.

Figure 5. The fast precipitation response for SALSA (P_{SALSA}) and the fast precipitation response for M7 (P_{M7}) for varying and constant injection strategies.

It is important to differentiate between the fast precipitation response and the change in precipitation. Since the fast precipitation response is calculated by dividing the TP values of each scenario with the TP values of the control data set, a 1 % precipitation anomaly in figure 5 corresponds to no change in precipitation. Which means that the precipitation is more abundant in scenarios where the constant injection strategy is used, especially for SALSA as seen in figure 5a. However, there is no clear pattern in M7 simulations in figure 5b.

4.3 Comparison of injection strategies

Figure 6a shows F_{TSR}, and 6b shows F_{TTR} for both aerosol modules and both injection strategies. These graphs contain the same information as figure 1, but both aerosol modules are shown in the same graph for easier comparison.

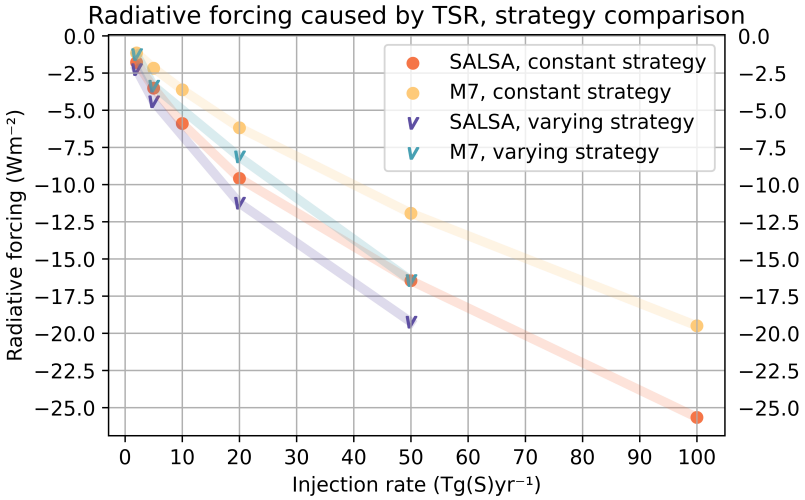

(a) F_{TSR} as a function of injection rate.

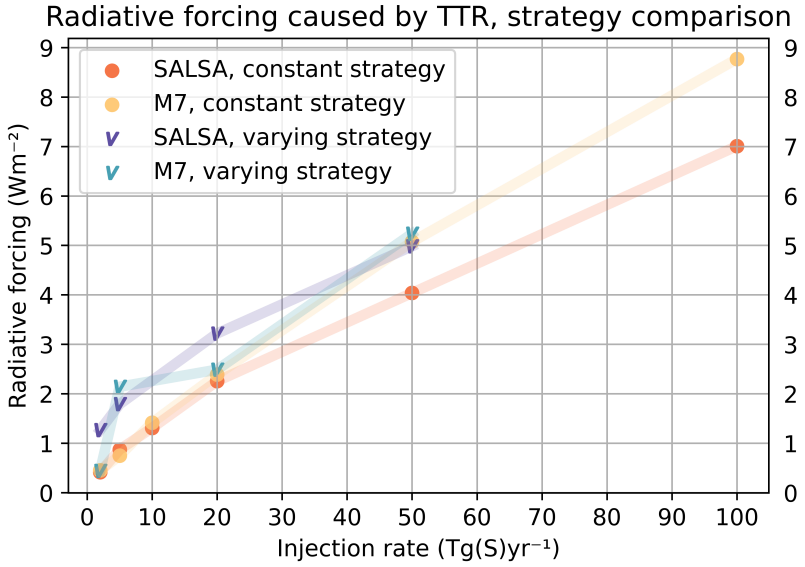

(b) F_{TTR} as a function of injection rate.

Figure 6. F_{TSR} and F_{TTR} with injection strategies and aerosol modules shown on the same graph.

The varying strategy is overall more effective than the constant strategy, as seen in figure 6. In figure 6a the varying M7 scenario is more effective than the constant M7

scenario, and this is also true while comparing the varying and constant scenarios of SALSA. The difference between scenarios grows larger with the increasing injection rate. Similarly the varying scenario is more effective for both aerosol modules in figure 6b.

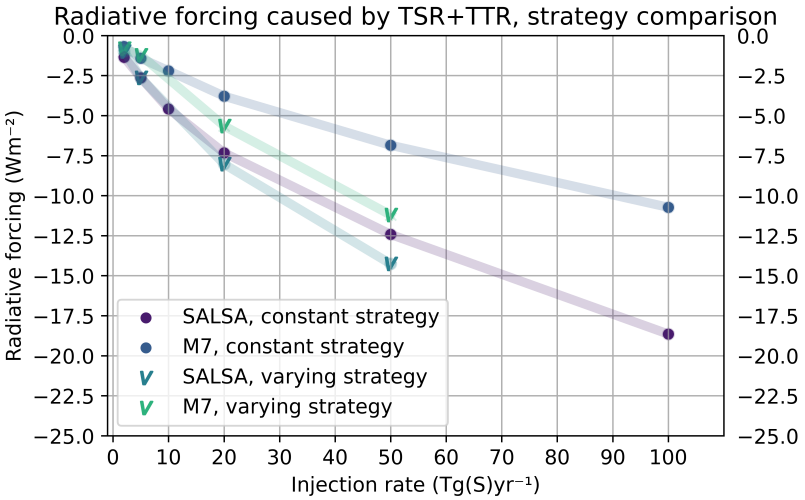

(a) F_{TOT} graph where the aerosol modules and strategies are shown separately.

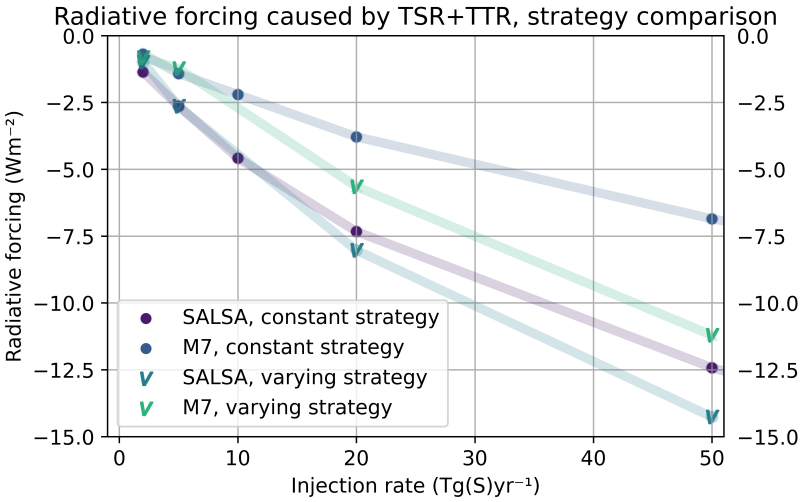

(b) Figure 7a with the x-axis restricted to 51 $\mathrm{Tg(S)/yr^{-1}}$ for easier comparison.

Figure 7. Comparison of different strategies for total radiative forcing.

For F_{TOT} with injection rates below 10 $\mathrm{Tg(S)yr^{-1}}$, both strategies provide similar results when controlling for aerosol module, however simulations done with SALSA produce more effective radiative forcing overall (figure 7). The varying strategy becomes more effective than the constant strategy at injection rates above 10 $\mathrm{Tg(S)yr^{-1}}$.

Precipitation responses P_{SALSA} and P_{M7} from figure 5 are shown in figure 8 with both aerosol modules and injection strategies in the same graph for easier comparison.

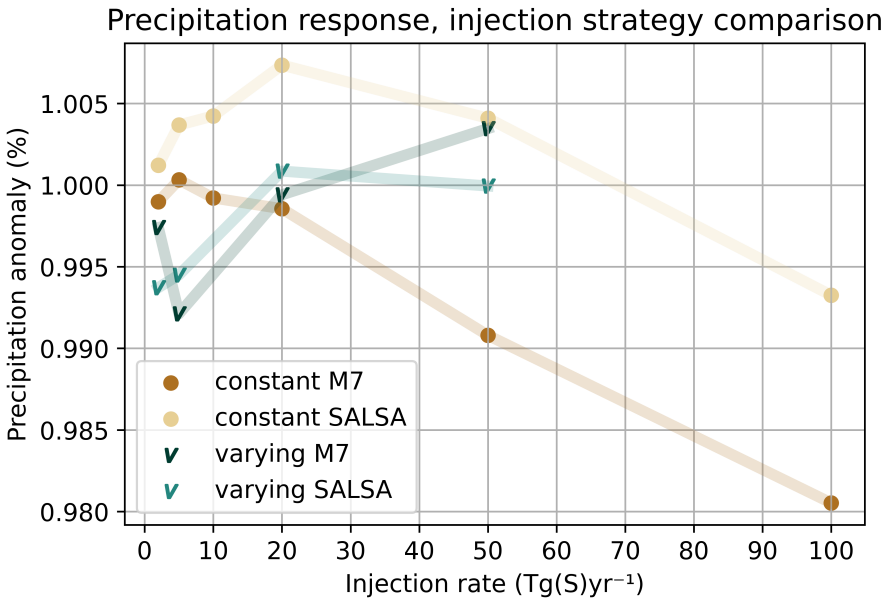

Figure 8. Fast precipitation response as a function of injection rate. Both injection strategies and aerosol modules are included.

There isn't a clear overall difference between the effect of varying and constant injection scenarios in figure 8. However when the injection rate is below 10 $\mathrm{Tg(S)yr}^{-1}$, the varying injection strategy produces a smaller precipitation response.

5 Conclusions

The choice of aerosol module affects both the radiative forcing and the precipitation response as seen in figures 6, 7 and 8. This can be explained by the way modal and sectional approaches handle particle size distributions and aerosol microphysics. As explained in section 3.2, SALSA uses a sectional approach with size bins and M7 uses lognormal modes to approximate the size distribution of particles. The modal approach in the M7 module tends to overestimate the condensational growth of particles. This causes the simulations done using M7 to have fewer but larger particles compared to simulations done with SALSA. [17][20]

Larger particles absorb radiation more effectively, resulting in more effective TTR forcing in simulations using M7. The amount of radiation scattered in the atmosphere is inversely proportional to the number of particles, so the M7 simulations have less effective TSR forcing. Since F_{TSR} is negative and F_{TTR} is positive, there is less radiative forcing overall in M7 simulations.

The fast precipitation response is inversely proportional to the radiation absorbed by the atmosphere, which means that P is inversely proportional to TTR forcing [21]. Since M7 simulations have more effective TTR forcing, the precipitation is reduced more due to the fast precipitation response simulated with this module. This is the case for the constant injection strategy in figure 8, however the results for the varying strategy are inconclusive.

Comparison of injection strategies for injection rates above $10\,\mathrm{Tg(S)yr^{-1}}$ in section 4.3 supports the hypothesis that a temporally and spatially varying injection strategy produces more effective total radiative forcing, and thus a stronger cooling effect (figure 7) . However there isn't a significant difference between the strategies below $10\,\mathrm{Tg(S)yr^{-1}}$ injection rates.

There is a more pronounced difference between varying and constant strategies when F_{TSR} and F_{TTR} are examined separately as in figure 6 where the varying strategy produces stronger radiative forcing. However this difference appears to even out for

injection rates below below $10\,\mathrm{Tg(S)yr^{-1}}$ when the top thermal radiation and top solar radiation data is summed.

In the case of CO_2 compensation (figure 4 and table 2 from appendix B), simulations done with SALSA produced similar results for both strategies when the injection rate was below $20\,\mathrm{Tg(S)yr^{-1}}$, and the difference between varying and constant scenarios were smaller overall in smaller injection rate scenarios. For example the CO_2 compensation rate corresponding to $2\,\mathrm{Tg(S)yr^{-1}}$ in simulations using aerosol fields simulated with M7 were 324 ppm for the constant strategy and 332 ppm for the varying strategy. However the difference between strategies was much larger in M7 scenarios with $20\,\mathrm{Tg(S)yr^{-1}}$ injection rate, the compensation rate being 581 ppm for the constant strategy and 826 ppm for the varying strategy.

The varying strategy appears to be more effective for larger injection rates, however rates above $20\,\mathrm{Tg(S)yr^{-1}}$ are considered unrealistic, and these simulations were subject to model stability issues discussed in section 3.5. Resolving these issues could also affect the difference between injection strategies at smaller injection rates, leading to more accurate conclusions about their effectivity.

References

[1] M. E. Mann. "Defining dangerous anthropogenic interference". In: *Proceedings of the National Academy of Sciences* 106.11 (2009), pp. 4065–4066. DOI: 10.1073/pnas.0901303106. eprint: https://www.pnas.org/doi/pdf/10.1073/pnas.0901303106. URL: https://www.pnas.org/doi/abs/10.1073/pnas.0901303106.

[2] G. T. (R. S. Davies. "Geoengineering the Climate: Science, Governance and Uncertainty". In: *Climate Law* 1.3 (2009). URL: https://royalsociety.org/topics-policy/publications/2009/geoengineering-climate/.

[3] A. Robock. "Volcanic eruptions and climate". In: *Reviews of Geophysics* 38.2 (2000), pp. 191–219. DOI: https://doi.org/10.1029/1998RG000054. eprint: https://agupubs.onlinelibrary.wiley.com/doi/pdf/10.1029/1998RG000054. URL: https://agupubs.onlinelibrary.wiley.com/doi/abs/10.1029/1998RG000054.

[4] D. Visioni et al. "What goes up must come down: impacts of deposition in a sulfate geoengineering scenario". In: *Environmental Research Letters* 15.9 (Aug. 2020), p. 094063. DOI: 10.1088/1748-9326/ab94eb. URL: https://dx.doi.org/10.1088/1748-9326/ab94eb.

[5] A. Laakso et al. "Dependency of the impacts of geoengineering on the stratospheric sulfur injection strategy – Part 1: Intercomparison of modal and sectional aerosol modules". In: *Atmospheric Chemistry and Physics* 22.1 (2022), pp. 93–118. DOI: 10.5194/acp-22-93-2022. URL: https://acp.copernicus.org/articles/22/93/2022/.

[6] A. Laakso et al. "Radiative and climate effects of stratospheric sulfur geoengineering using seasonally varying injection areas". In: *Atmospheric Chemistry and Physics* 17.11 (2017), pp. 6957–6974. DOI: 10.5194/acp-17-6957-2017. URL: https://acp.copernicus.org/articles/17/6957/2017/.

[7] J. Hansen, M. Sato, and R. Ruedy. "Radiative forcing and climate response". In: *Journal of Geophysical Research: Atmospheres* 102.D6 (1997), pp. 6831–6864. DOI: https://doi.org/10.1029/96JD03436. eprint: https://agupubs.

onlinelibrary.wiley.com/doi/pdf/10.1029/96JD03436. URL: https://agupubs.onlinelibrary.wiley.com/doi/abs/10.1029/96JD03436.

[8] J. M. Gregory et al. "A new method for diagnosing radiative forcing and climate sensitivity". In: *Geophysical Research Letters* 31.3 (2004). DOI: https://doi.org/10.1029/2003GL018747. eprint: https://agupubs.onlinelibrary.wiley.com/doi/pdf/10.1029/2003GL018747. URL: https://agupubs.onlinelibrary.wiley.com/doi/abs/10.1029/2003GL018747.

[9] E. J. Rohling et al. "Making sense of palaeoclimate sensitivity". In: *Nature* 491 (Nov. 2012), pp. 683–691. DOI: https://doi.org/10.1038/nature11574.

[10] G. Myhre et al. "New estimates of radiative forcing due to well mixed greenhouse gases". In: *Geophysical Research Letters* 25.14 (1998), pp. 2715–2718. DOI: https://doi.org/10.1029/98GL01908. eprint: https://agupubs.onlinelibrary.wiley.com/doi/pdf/10.1029/98GL01908. URL: https://agupubs.onlinelibrary.wiley.com/doi/abs/10.1029/98GL01908.

[11] T. Andrews and P. M. Forster. "The transient response of global-mean precipitation to increasing carbon dioxide levels". In: *Environmental Research Letters* 5.2 (June 2010), p. 025212. DOI: 10.1088/1748-9326/5/2/025212. URL: https://dx.doi.org/10.1088/1748-9326/5/2/025212.

[12] A. Laakso et al. "Differing precipitation response between solar radiation management and carbon dioxide removal due to fast and slow components". In: *Earth System Dynamics* 11.2 (2020), pp. 415–434. DOI: 10.5194/esd-11-415-2020. URL: https://esd.copernicus.org/articles/11/415/2020/.

[13] M. G. Schultz et al. "The chemistry–climate model ECHAM6.3-HAM2.3-MOZ1.0". In: *Geoscientific Model Development* 11.5 (2018), pp. 1695–1723. DOI: 10.5194/gmd-11-1695-2018. URL: https://gmd.copernicus.org/articles/11/1695/2018/.

[14] R. Döscher et al. "The EC-Earth3 Earth system model for the Coupled Model Intercomparison Project 6". In: *Geoscientific Model Development* 15.7 (2022), pp. 2973–3020. DOI: 10.5194/gmd-15-2973-2022. URL: https://gmd.copernicus.org/articles/15/2973/2022/.

[15] Y. Zhang et al. "Impact of aerosol size representation on modeling aerosol-cloud interactions". In: *Journal of Geophysical Research: Atmospheres* 107.D21 (2002), AAC 4-1-AAC 4–17. DOI: https://doi.org/10.1029/2001JD001549. eprint: https://agupubs.onlinelibrary.wiley.com/doi/pdf/10.1029/

2001JD001549. URL: https://agupubs.onlinelibrary.wiley.com/doi/abs/10.1029/2001JD001549.

[16] E. Vignati, J. Wilson, and P. Stier. "M7: An efficient size-resolved aerosol microphysics module for large-scale aerosol transport models". In: *Journal of Geophysical Research: Atmospheres* 109.D22 (2004). DOI: https://doi.org/10.1029/2003JD004485. eprint: https://agupubs.onlinelibrary.wiley.com/doi/pdf/10.1029/2003JD004485. URL: https://agupubs.onlinelibrary.wiley.com/doi/abs/10.1029/2003JD004485.

[17] H. Kokkola et al. "SALSA2.0: The sectional aerosol module of the aerosol–chemistry–climate model ECHAM6.3.0-HAM2.3-MOZ1.0". In: *Geoscientific Model Development* 11.9 (2018), pp. 3833–3863. DOI: 10.5194/gmd-11-3833-2018. URL: https://gmd.copernicus.org/articles/11/3833/2018/.

[18] *Puhti - Services for Research - CSC Company Site*. https://research.csc.fi/-/puhti. Accessed: 2023-03-08.

[19] A. Laakso. "Dependency of the impacts of geoengineering on the stratospheric sulfur injection strategy part 2: How changes in the hydrological cycle depend on injection rates and model?" In: *[Unpublished manuscript]* ().

[20] Y. Zhang et al. "Simulation of Aerosol Dynamics: A Comparative Review of Algorithms Used in Air Quality Models". In: *Aerosol Science and Technology* 31.6 (1999), pp. 487–514. DOI: 10.1080/027868299304039. eprint: https://doi.org/10.1080/027868299304039. URL: https://doi.org/10.1080/027868299304039.

[21] L. Duan et al. "Comparison of the Fast and Slow Climate Response to Three Radiation Management Geoengineering Schemes". In: *Journal of Geophysical Research: Atmospheres* 123.21 (2018), pp. 11, 980–12, 001. DOI: https://doi.org/10.1029/2018JD029034. eprint: https://agupubs.onlinelibrary.wiley.com/doi/pdf/10.1029/2018JD029034. URL: https://agupubs.onlinelibrary.wiley.com/doi/abs/10.1029/2018JD029034.

[22] K. Caldeira, B. Govindasamy, and L. Cao. "The Science of Geoengineering". In: *Annual Review of Earth and Planetary Sciences* 41 (May 2012). DOI: 10.1146/annurev-earth-042711-105548.

A Linear regression graphs

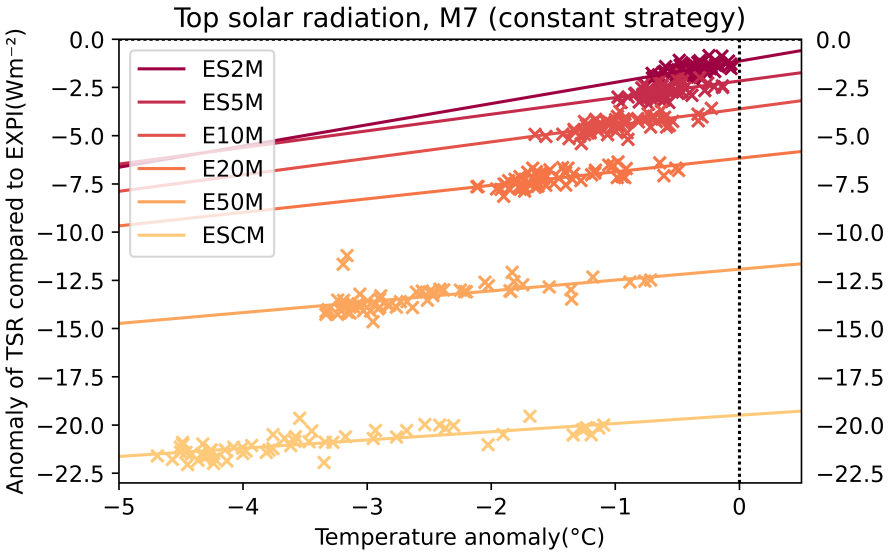

(a) Linear regression of TSR against T2M, M7 aerosol module.

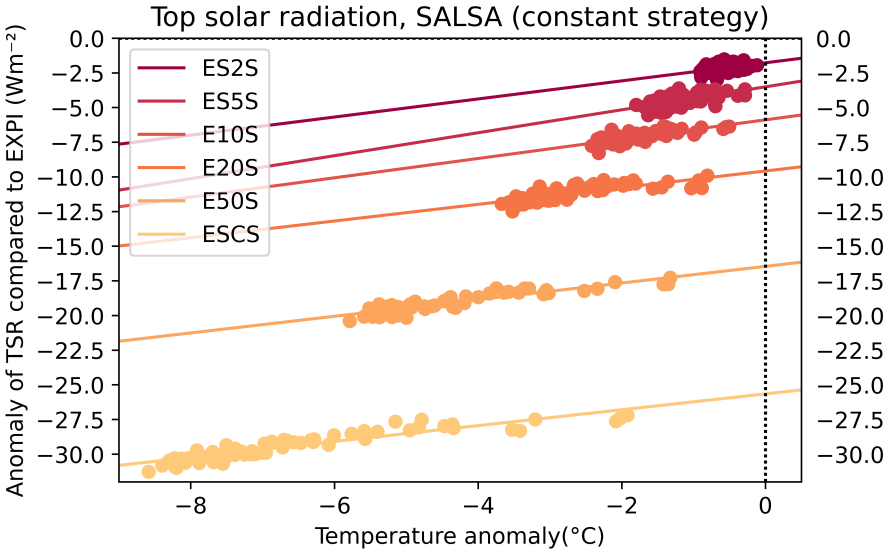

(b) Linear regression of TSR against T2M, SALSA aerosol module.

Figure 9. Linear regression of TSR and TTR against T2M with data obtained from the constant injection scenarios. Results for SALSA and M7 are shown separately. Data set labels are explained in table 1.

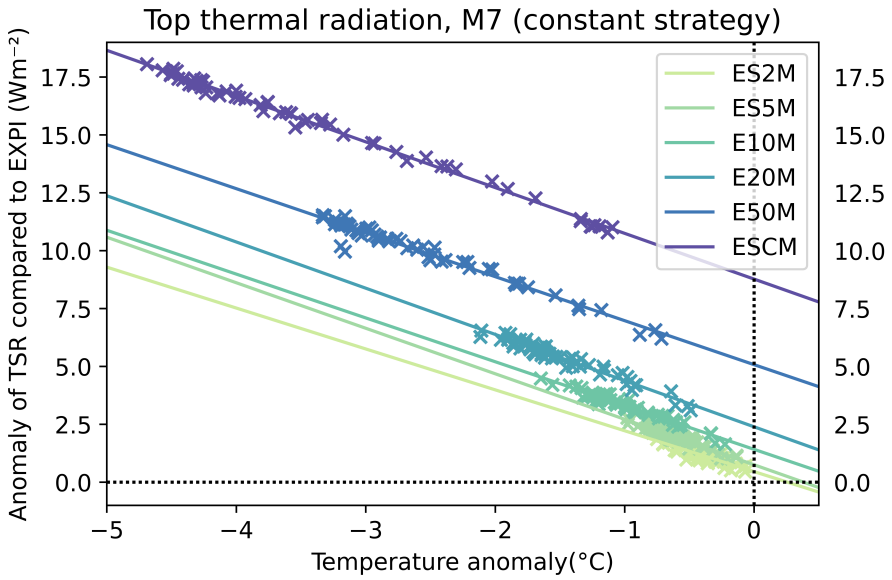

(a) Linear regression of TTR against T2M, M7 aerosol module.

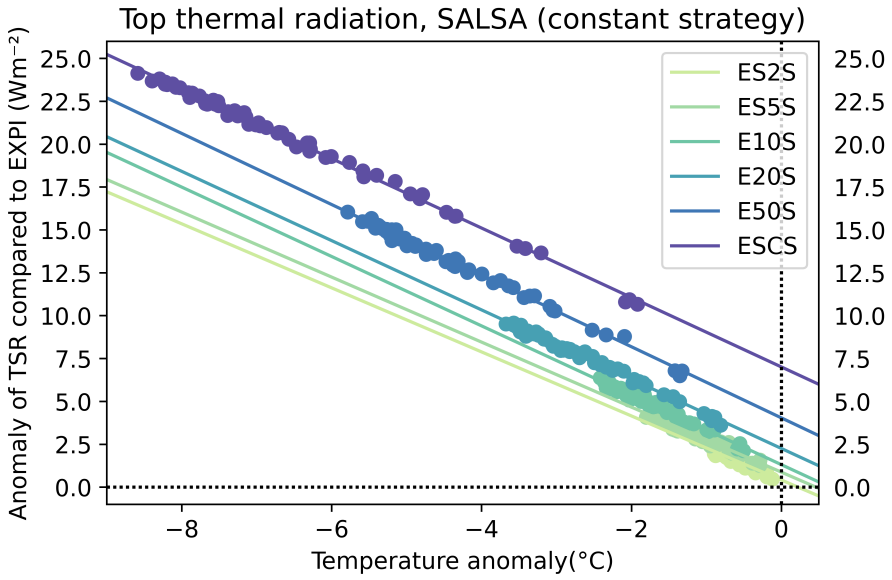

(b) Linear regression of TTR against T2M, SALSA aerosol module.

Figure 10. Linear regression of TSR and TTR against T2M with data obtained from the constant injection scenarios. Results for SALSA and M7 are shown separately. Data set labels are explained in table 1.

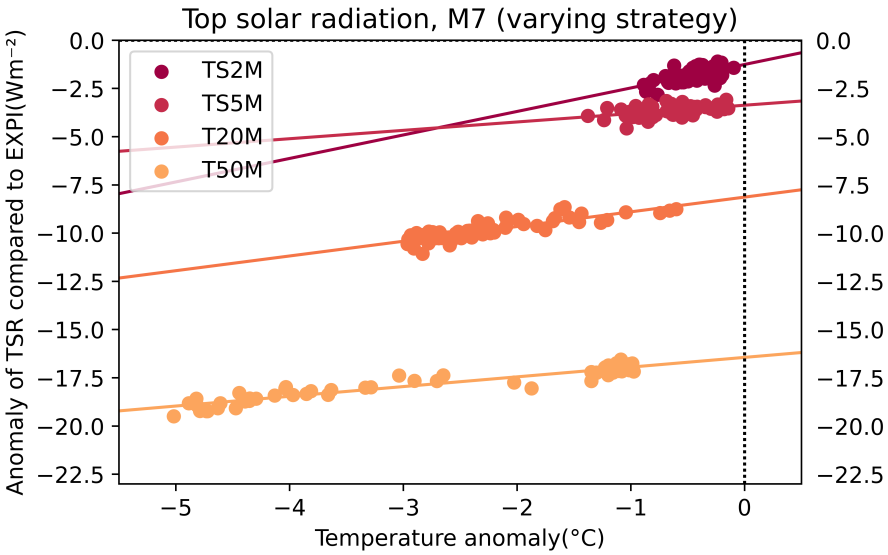

(a) Linear regression of TSR against T2M, M7 aerosol module.

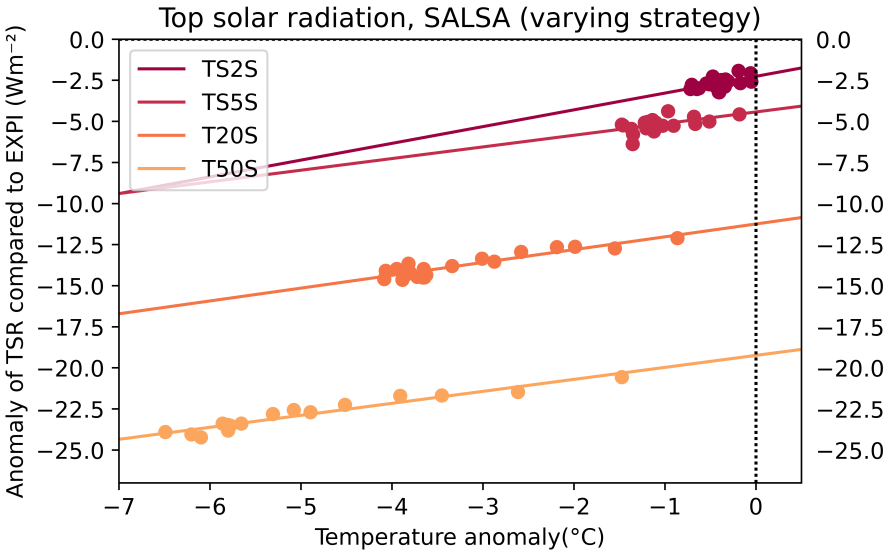

(b) Linear regression of TSR against T2M, SALSA aerosol module.

Figure 11. Linear regression of TSR and TTR against T2M with data obtained from the varying injection scenarios. Results for SALSA and M7 are shown separately. Data set labels are explained in table 1.

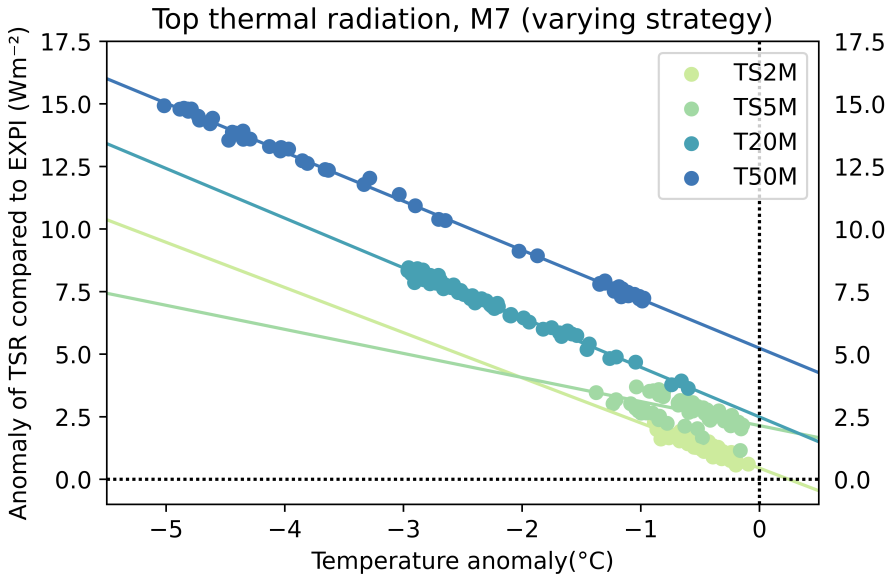

(a) Linear regression of TTR against T2M, M7 aerosol module.

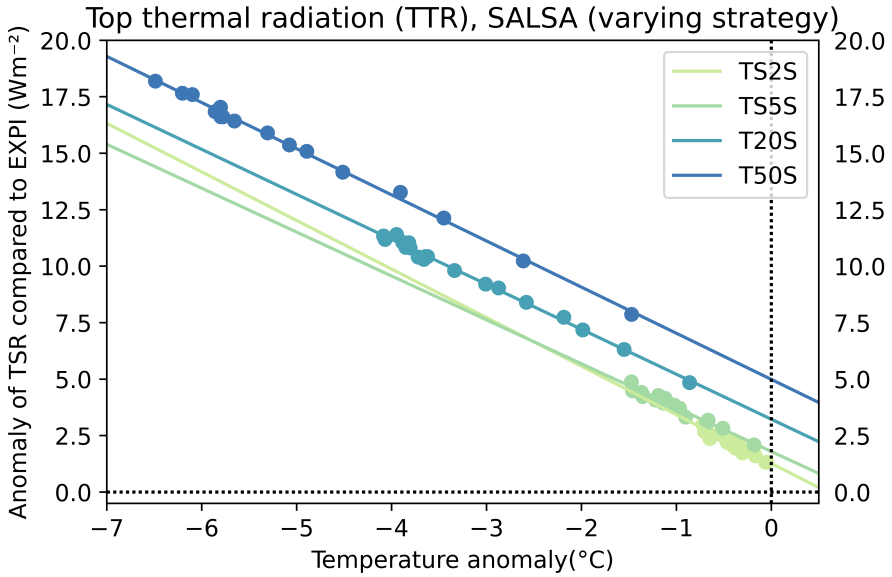

(b) Linear regression of TTR against T2M, SALSA aerosol module.

Figure 12. Linear regression of TSR and TTR against T2M with data obtained from the varying injection scenarios. Results for SALSA and M7 are shown separately. Data set labels are explained in table 1.

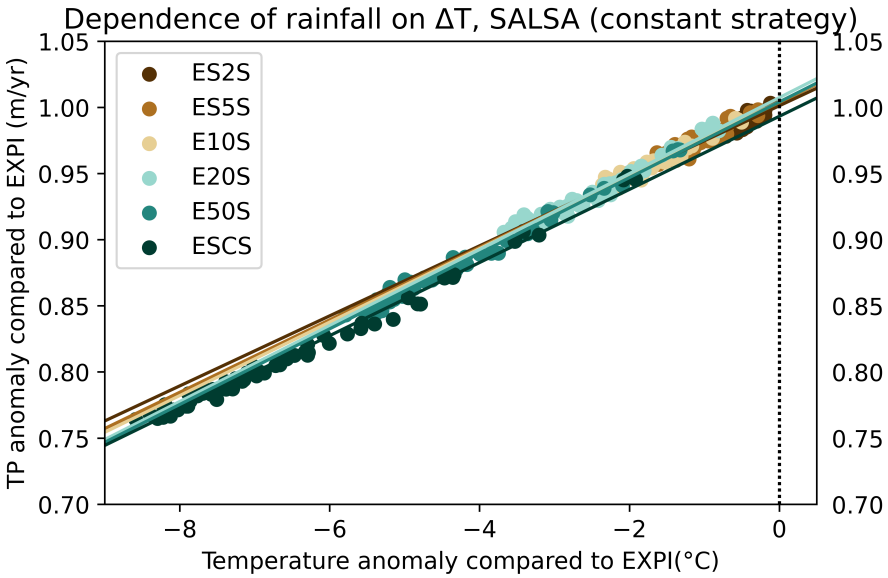

(a) Linear regression of TP against T2M, constant strategy.

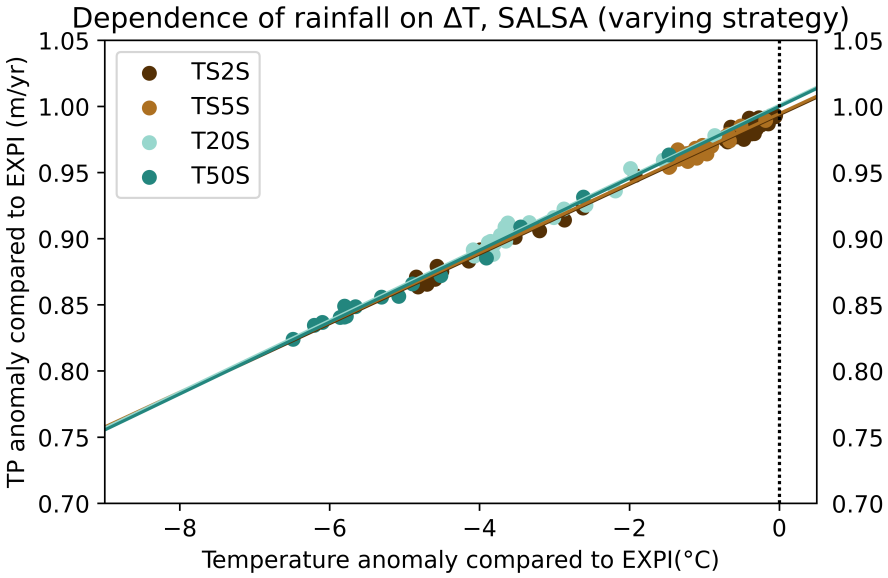

(b) Linear regression of TTR against T2M, varying strategy.

Figure 13. Linear regression of TP against T2M with data obtained from aerosol fields simulated with SALSA. Data set labels are explained in table 1.

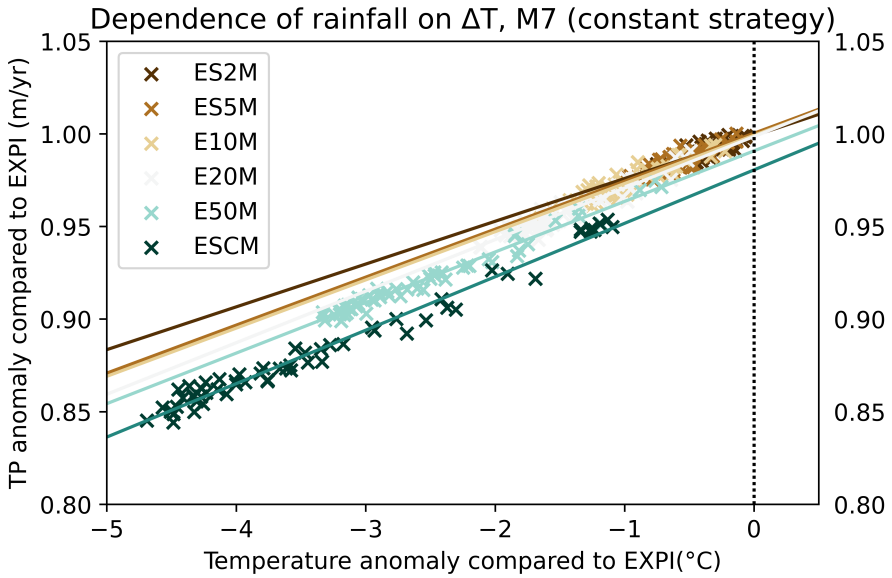

(a) Linear regression of TP against T2M, constant strategy.

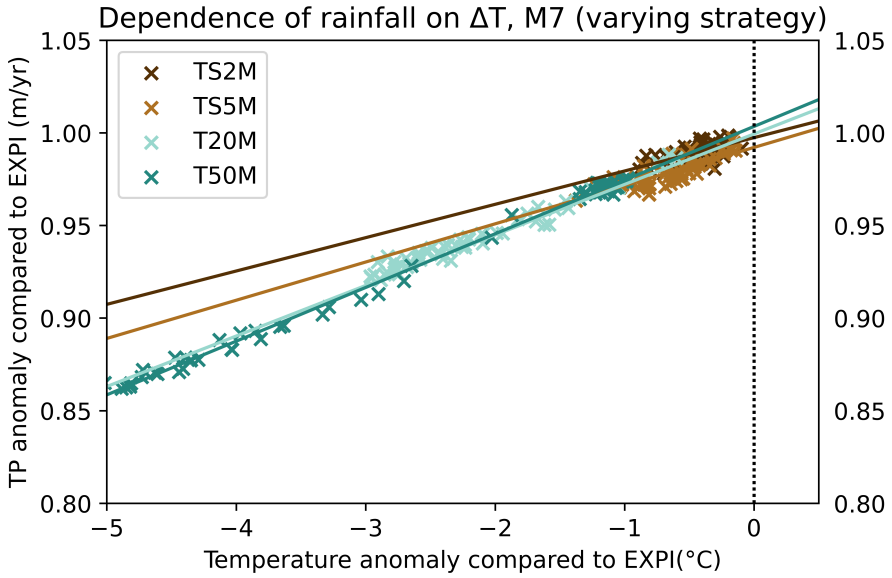

(b) Linear regression of TP against T2M, varying strategy.

Figure 14. Linear regression of TP against T2M with data obtained from aerosol fields simulated with M7. Data set labels are explained in table 1.

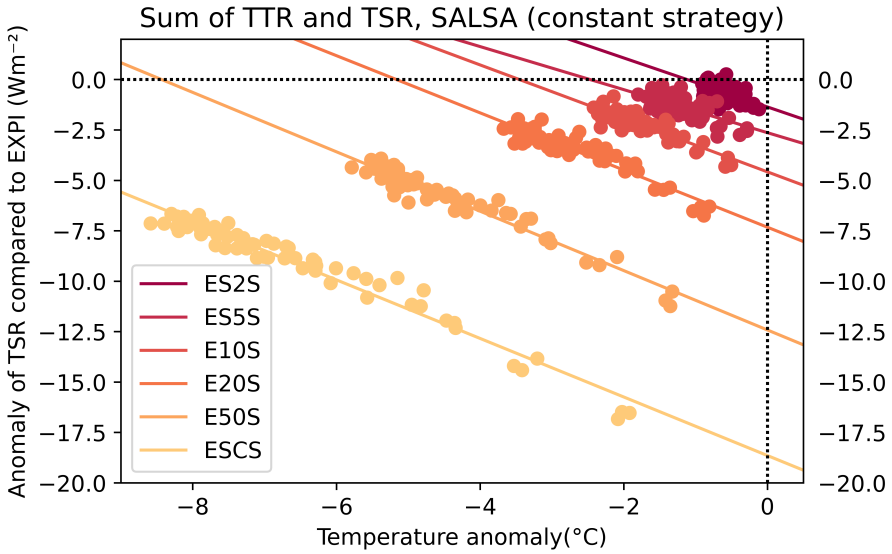

(a) Linear regression of TSR+TTR against T2M, SALSA aerosol module.

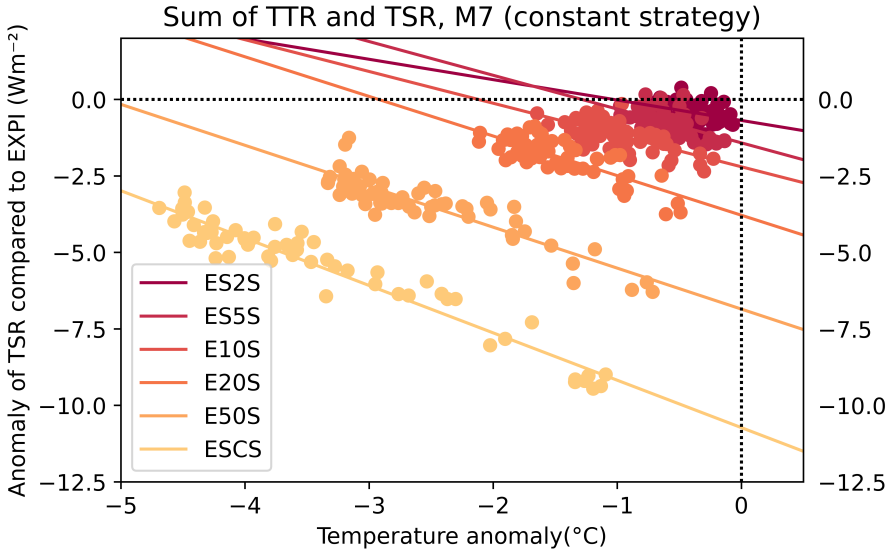

(b) Linear regression of TSR+TTR against T2M, M7 aerosol module.

Figure 15. Linear regression of TSR+TTR against T2M with data obtained from the constant injection scenarios. Results for SALSA and M7 are shown separately. Data set labels are explained in table 1.

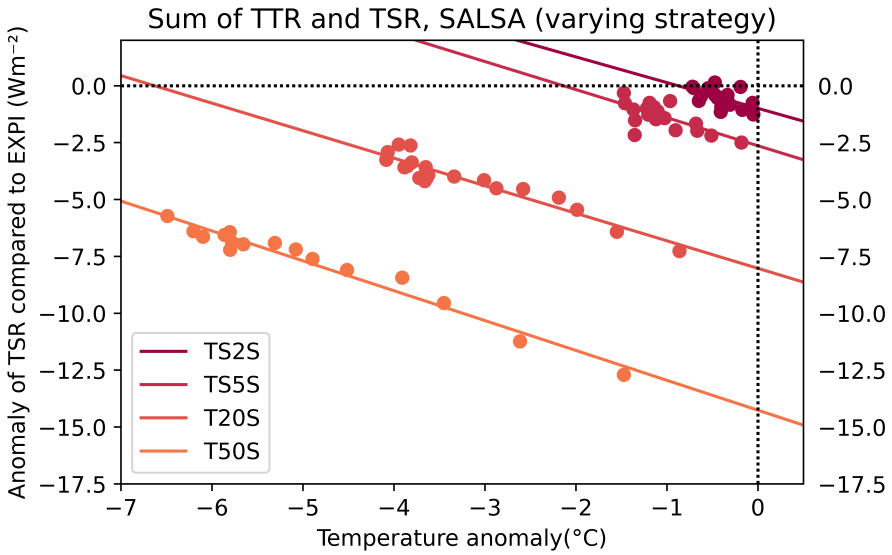

(a) Linear regression of TSR+TTR against T2M, SALSA aerosol module.

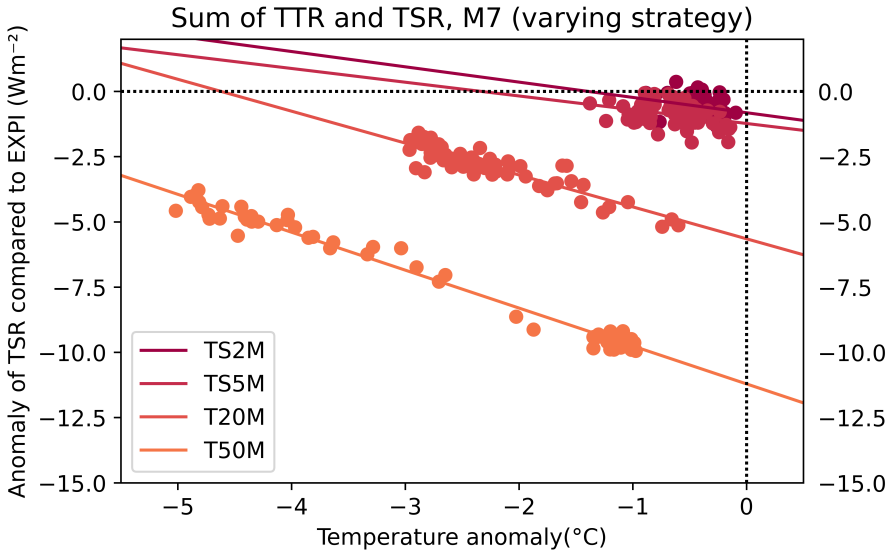

(b) Linear regression of TSR+TTR against T2M, M7 aerosol module.

Figure 16. Linear regression of TSR+TTR against T2M with data obtained from the varying injection scenarios. Results for SALSA and M7 are shown separately. Data set labels are explained in table 1.

B Numerical values of CO_2 compensation shown in figure 4

Table 2. CO_2 compensation calculated with equation (5) using data from table 1, and figures 2 and 3b.

Aerosol Module	Strategy	Injection rate Tg(S)yr^{-1}	CO_2 compensation (ppm)
M7	Constant	2	324
M7	Constant	5	372
M7	Constant	10	431
M7	Constant	20	581
M7	Constant	50	1036
M7	Constant	100	2152
M7	Varying	2	332
M7	Varying	5	359
M7	Varying	20	826
M7	Varying	50	2356
SALSA	Constant	2	368
SALSA	Constant	5	468
SALSA	Constant	10	675
SALSA	Constant	20	1133
SALSA	Constant	50	2962
SALSA	Constant	100	9584
SALSA	Varying	2	343
SALSA	Varying	5	468
SALSA	Varying	20	1293
SALSA	Varying	50	4192